Investigations of the pH-Dependent Adsorption of Uranyl Species on Phosphorylated Cellulose-Nanocrystal Ferrihydrite: Insights from Combined Raman Spectroscopy and Computational Analyses

Tanmayaa Nayak[1], Sujan Manna[1], Ankita Narwal[2], Bijesh Kumar Malla[1], Sonali Seth[1], Sandeep K Reddy[3], Sharma S. R. K. C. Yamijala*[2], and Thalappil Pradeep*[1]

[1]DST Unit of Nanoscience (DST UNS) and Thematic Unit of Excellence (TUE), Department of Chemistry, Indian Institute of Technology Madras, Chennai 600 036, India

[2]Department of Chemistry, Indian Institute of Technology Madras, Chennai 600 036, India

[3]Centre for Computational and Data Science, Indian Institute of Technology Kharagpur, Kharagpur, West Bengal, 721302, India

*Corresponding authors

Email: yamijala@smail.iitm.ac.in

*Email: pradeep@iitm.ac.in

Contents

Total number of pages: 16

Total number of figures: 13

Total number of tables: 2

Total number of equations: 4

Table of Contents

Items	Title	Page No.
	Materials	S2
	Instrumentation	S2-S3
	Computational Details	S3-S6
Figure S1	Comparative FTIR spectra of uranyl stock solution prepared at pH 5.0, 7.5 and 9.0 (pH are adjusted by HNO_3/Na_2CO_3).	S7
Figure S2	FTIR spectra of PCNCFH and U(VI) adsorbed PCNCFH (U-PCNCFH) at pH 7.5.	S7
Figure S3	Comparative Raman spectral peak fitting analyses for the uranyl solution collected at λ_{ex} = 633 and 785 for pH 7.5, and pH 9.0.	S8

Figure S4	Raman spectra for the various concentrations of U(VI) stock solutions at pH 5.0 and it's corresponding peak area vs concentration graph.	S8-S9
Figure S5	Raman spectra for the various concentrations of U(VI) stock solutions at pH 7.5 and it's corresponding peak area vs concentration graph.	S9
Figure S6	Raman spectra for the various concentrations of U(VI) stock solutions at pH 9.0 and it's corresponding peak area vs concentration graph.	S10
Figure S7	Time-dependent Raman spectra of the interaction of PCNCFH with U(VI) at pH - 7.5, and pH - 9.0.	S10-S11
Figure S8	Pseudo-first-order kinetics graph for PCNCFH at (a) pH 5.0, (b) pH 7.5, and (c) pH 9.0.	S11
Figure S9	Zeta potential as a function of pH (range 5 -10) for PCNCFH particles in water.	S11
Figure S10	Bulk hexagonal conventional unit cell (containing 6 formula units) of α-Fe_2O_3.	S12
Figure S11	Top and side views of the optimised $[UO_2(CO_3)_3]^{4-}$ complex and $[(UO_2)_3(O)(OH)_3(H_2O)_6]^+$ complex.	S12
Figure S12	Side views of the optimised $[UO_2(CO_3)_3]^{4-}$ and $[(UO_2)_3(O)(OH)_3(H_2O)_6]^+$ complexes adsorbed onto the α-Fe_2O_3(0001) surface.	S13
Figure S13	Energy profiles of $[UO_2(CO_3)_3]^{4-}$ and $[(UO_2)_3(O)(OH)_3(H_2O)_6]^+$ complexes adsorbed onto the α-Fe_2O_3(0001) surface.	S13
Table S1	Comparative U(VI) removal efficiency of PCNC and PCNCFH, calculated from ICPMS data	S13
Table S2	Binding energies with varying *Hubbard U* values for uranium complexes on α-Fe_2O_3(0001).	S14
Equations used	Equations used in the main text	S14-S15
	References	S15-S16

Materials

Uranyl nitrate hexahydrate salt ($UO_2(NO_3)_2.6H_2O$) was purchased Thomas Baker (Chemicals) Ltd. Sodium carbonate (Na_2CO_3) and HNO_3 were purchased from Rankem Glasswares and Chemicals Pvt.Ltd., India respectively. Phosphorylated cellulose nanocrystal- ferrihydrite (PCNCFH) was synthesized in the laboratory. For the synthesis of PCNCFH, $FeCl_3 \cdot 6H_2O$, STMP, and Na_2SO_4 were obtained from RANKEM Glasswares, Sigma Aldrich, and Chemicals Pvt. Ltd., India respectively. All chemicals were of analytical grade and were used without further purification. Deionized (DI) water was used throughout the experiments.

Instrumentation

High Resolution Transmission Electron Microscopy (HRTEM) - TEM images were obtained using a JEOL 3010 instrument fitted with an ultra-high resolution (UHR) polepiece, operating at an accelerating voltage of 200 kV. For high-resolution TEM (HRTEM) analysis, the nanocomposite was first dispersed in water, and the suspension was subsequently drop-cast onto carbon-coated copper grids. The prepared grids were left to dry under ambient conditions at room temperature for imaging.

Infrared (IR) – IR spectra are collected using PerkinElmer IR instrument within the range of 400-4000 cm^{-1}.

Raman Spectroscopy - Raman spectroscopy was performed using CRM Alpha 300 S microRaman spectrometer of WiTec GmbH (Germany). A glass slide with a cavity (which can hold 100 µL of the sample solution) was mounted on the piezoelectric scan stage of the setup. The spectra (for pH 7.53 and pH 9.01) were collected at 633 nm laser excitation. The spectra for pH 5.01 were collected using a Lightnovo miniRaman handheld spectrometer with an excitation wavelength of 785 nm for all measurements. Integration times (t_{int}) for spectra collected using λ_{ex} = 633 and 785 nm were 5 and 20 s, respectively. Laser powers (P) were 10−11 and 90 mW, respectively. The background subtraction of the spectrum was done using a second-order polynomial. All reported Raman spectra represent an average of 10 spectra, which were background corrected using a blank (water) Raman spectrum, and intensities were corrected by dividing spectral counts by laser power and integration time. To compare spectral intensities collected on the various Raman detectors, an ethanol standard was used so that instrument correction factors (from detectors and excitation wavelengths) were estimated. Briefly, Raman bands from the symmetric stretching mode of uranyl UO_2^{2+} were analyzed using a peak analysis protocol (Casa XPS) using data between 750 - 880 cm^{-1}. Then, the second derivative of this spectral window were smoothed using the Savitzky-Golay filter (8 points) in Origin 2025b. Both Gaussian and Lorentzian functions were used for spectral analysis. Species were determined by setting vibrational frequency windows expected from the literature.[1,2] Fwhm (Γ) values for all uranyl species were set between 13 - 20 cm^{-1}.

Computational Details - All electronic structure calculations and Born–Oppenheimer molecular dynamics (BOMD) simulations were performed within the Kohn–Sham density functional theory (DFT) framework.[3] The exchange–correlation effects were described using the Perdew–Burke–Ernzerhof (PBE) functional, combined with molecularly optimized double-

ζ valence polarized short-range (DZVP-SR) basis sets, as implemented in the CP2K software package.[4,5] For the auxiliary plane-wave basis, a kinetic energy cutoff of 300 Ry and a reference grid cutoff of 60 Ry were used.[6,7] The core–valence interactions for Fe, H, O, C, and U atoms were modeled using Goedecker–Teter–Hutter (GTH) pseudopotentials, which are compatible with the selected basis sets.[8] Long-range dispersion interactions were accounted for via Grimme's D3 correction scheme.[9] Given the relatively large size of the simulation cell, Brillouin zone sampling was limited to the Γ-point. Structural optimizations for the uranium complexes and α-Fe_2O_3 surfaces were performed until the forces on all atoms were smaller than 0.02 eV/Å, and the energy convergence criterion for the self-consistent field (SCF) cycles was set to 10^{-5} eV. Spin polarization was included throughout all calculations to accurately describe the magnetic ordering of Fe^{3+} centers in α-Fe_2O_3. A 4 × 4 supercell of hexagonal α-Fe_2O_3, measuring 20.36 Å × 20.36 Å × 32.55 Å and containing 96 Fe and 144 O atoms, was considered to study the adsorption of uranium-based complexes, where the large supercell ensures minimal lateral interactions between periodic images of the adsorbate.

Taking into account the strong correlation between 3d-electrons of the Fe atom, it is well-established that a Hubbard *U* term acting on the Fe 3d atoms is required in addition to the standard density functional to get an accurate description of the electronic structure. To account for the strong on-site Coulomb interactions associated with localized *d* and *f* electrons, which are not adequately described by standard GGA or LDA functionals, we employed the DFT+U approach. Specifically, the simplified Dudarev scheme,[10] as implemented in CP2K/Quickstep, was used, wherein the Hubbard correction is introduced through a single effective parameter $U_{eff} = U - J$, with U and J representing the on-site Coulomb and exchange interaction parameters, respectively. For simplicity, U_{eff} is generally referred to in literature as "*U*",[11] and the same convention is adopted here.

Based on prior literature, a Hubbard *U* value of 5 eV was applied to Fe 3d states, which is known to yield an accurate description of the magnetic and electronic properties of α-Fe_2O_3.[12–14] Uranium in the studied complexes predominantly exists in the hexavalent oxidation state, corresponding to a $5f^0$ electronic configuration. Because U(VI) lacks partially occupied 5f orbitals, strong on-site correlation effects are expected to be minimal. Hence, energies were computed both using a small on-site Coulomb parameter (U = 2 eV) on Uranium and without any additional Hubbard correction (U = 0 eV). This approach is consistent with earlier

computational studies on the U(VI) systems. For example, Grabias *et al.*[15] employed $U = 0$ eV for uranium and successfully described the structure and stability of U(VI) hydroxyl species.

In addition, the widely used value of $U = 4.0$ eV was derived specifically from spectroscopic measurements of UO_2, a U(IV) system,[16,17] and its transferability to other uranium species and oxidation states is not guaranteed.[18] Indeed, earlier estimates for neutral uranium atoms yielded considerably lower values for U (2.3 eV[19] and 1.9 eV[20]), highlighting the strong system dependence even within uranium chemistry. Also, Beridze and Kowalski[18] demonstrated that the U value depends strongly on both the oxidation state and the chemical environment of uranium. For instance, the U values that they derived for uranium halides, oxides, and oxyhalides span a narrow range: UO_3 = 2.6 eV, UCl_6 = 2.2 eV, UOF_4 = 2.8 eV, UF_6 = 3.1 eV, and are consistently smaller by approximately 2 eV than the widely adopted UO_2-derived value of 4.0 eV. *All these reports justify the small U correction (U = 0-2 eV) employed in the present study.* Initial structures of the surface–adsorbate systems were generated using the PACKMOL software.[21] BOMD simulations were conducted in the canonical (NVT) ensemble at 300 K with a time step of 1 fs, and the temperature was maintained using a Nosé–Hoover chain thermostat.[22,23] A vacuum gap of at least 15 Å was introduced along the surface normal to eliminate interactions between repeated slabs. For each system, the NVT simulations were conducted for about 2.5 ps to identify a representative low-energy adsorption geometry of the uranium complex on the α-Fe_2O_3(0001) surface. The minimum-energy configuration sampled during the trajectory was extracted and subsequently optimized using spin-polarized DFT without any Hubbard correction ($U = 0$). After full relaxation, single-point SCF calculations were performed on the optimized structures by introducing the appropriate on-site Coulomb corrections (Hubbard correction). These Hubbard *U*–corrected energies were then used for calculating the binding energies.

The binding energy (E_{bind}) of a uranium complex on an α-Fe_2O_3(0001) surface was calculated using the formula, $E_{bind} = E_{surface+uc} - E_{surface} - E_{uc}$, where $E_{surface+uc}$ and $E_{surface}$ are the total energies of the uranium complex adsorbed on α-Fe_2O_3(0001) surface and the pristine α-Fe_2O_3(0001) surface, respectively, and E_{uc} is the energy of an isolated uranium complex. Visualization of trajectories and generation of molecular structures were performed using VMD[24] and VESTA.

Regarding solvation treatment, the uranyl complexes were handled according to their intrinsic coordination chemistry. The hydroxo complex, $[(UO_2)_3(O)(OH)_3(H_2O)_6]^+$, incorporates six

explicit inner-sphere water molecules as part of its primary coordination shell, which were retained in all DFT and BOMD simulations, providing explicit quantum mechanical treatment of first-shell interactions. The carbonato complex, $[UO_2(CO_3)_3]^{4-}$, does not coordinate with water molecules in its primary sphere and was treated accordingly. No implicit continuum solvent model was applied beyond the first coordination shell in either case.

We note that the absence of extended solvation may affect the absolute adsorption energies, primarily due to the lack of long-range dielectric screening and bulk solvent stabilization. In particular, solvation could influence the relative stabilization of charged species and interfacial hydrogen-bonding networks. However, since all systems are treated within the same computational framework and the primary coordination environment is explicitly considered, the relative adsorption trends and comparative reactivity are expected to remain valid. A fully explicit solvation treatment would require substantially larger system sizes, longer simulation times, and systematic sampling of solvent configurations, which are beyond the scope of the present study.

Visualization of trajectories and generation of molecular structures were performed using VMD[25] and VESTA.

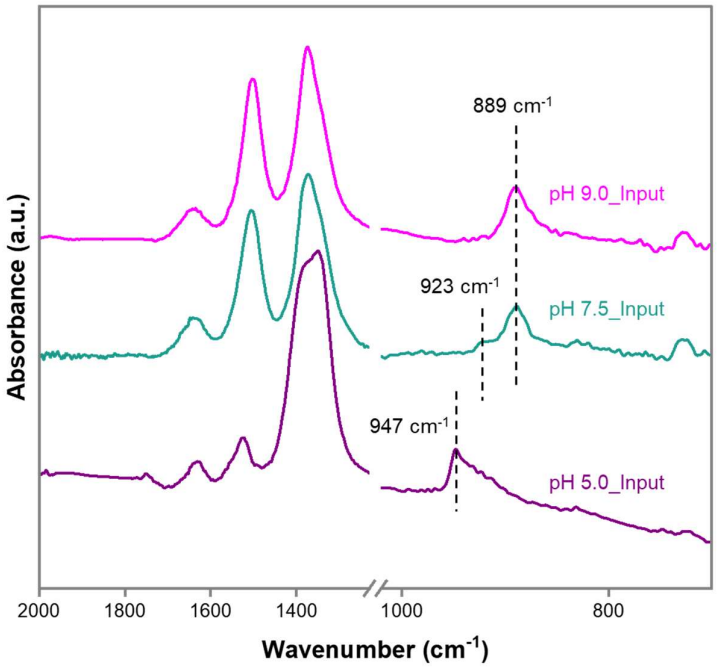

Figure S1. Comparative FTIR spectra of uranyl stock solution prepared at pH 5.0, 7.5 and 9.0 (pH are adjusted by HNO_3/Na_2CO_3).

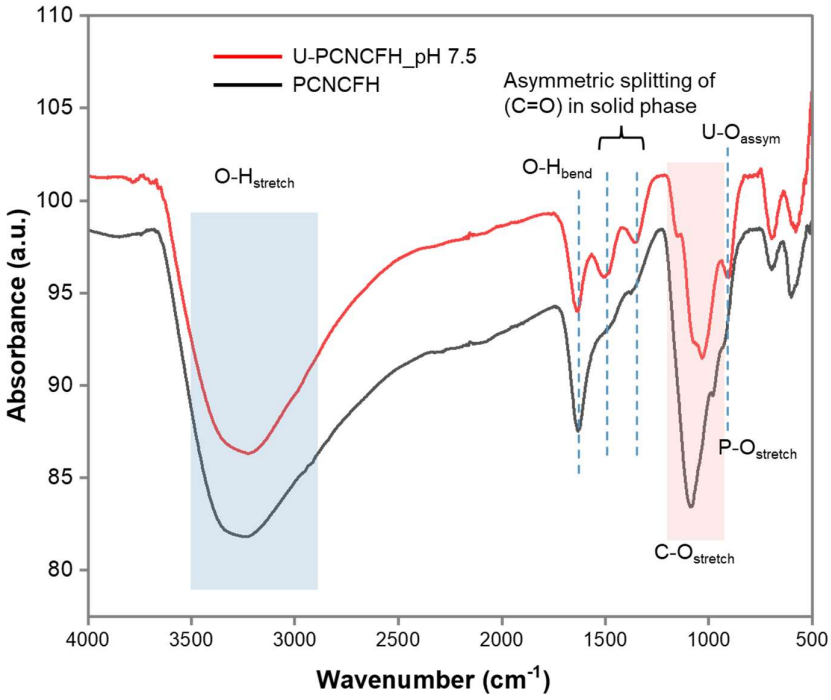

Figure S2. FTIR spectra of PCNCFH and U(VI) adsorbed PCNCFH (U-PCNCFH) at pH 7.5.

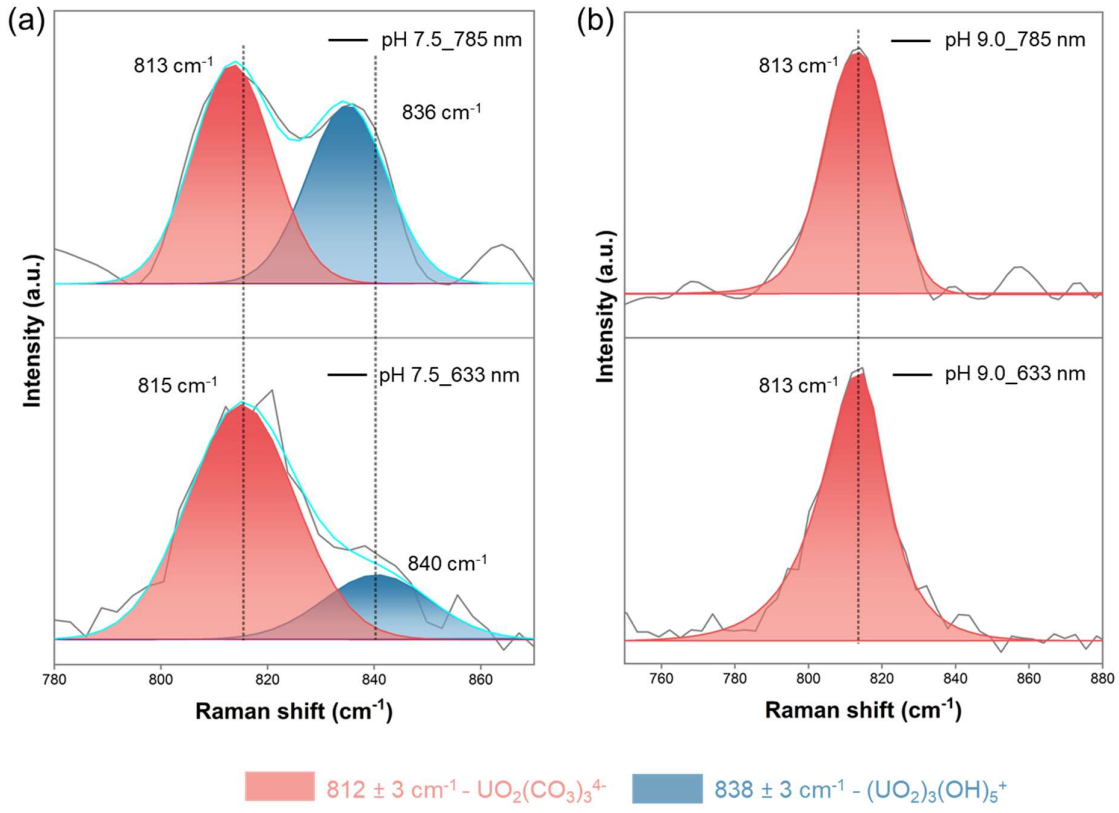

Figure S3. Comparative Raman spectral peak fitting analyses for the uranyl solution collected at λ_{ex} = 633 and 785 for (a) pH 7.5, (b) pH 9.0.

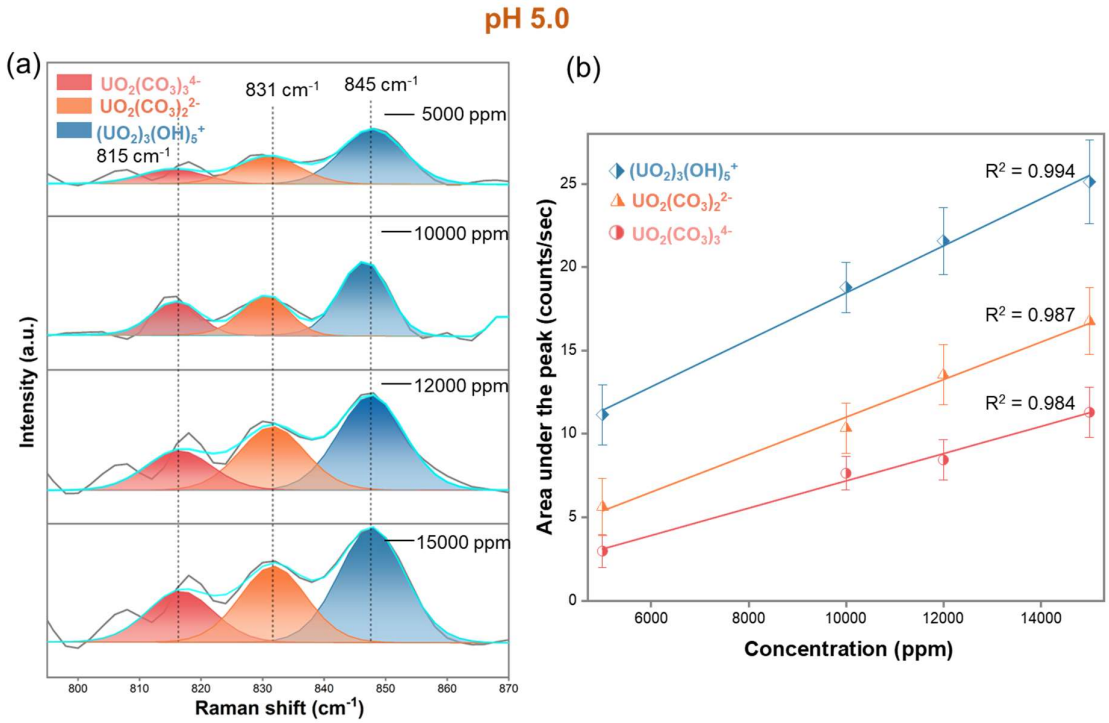

Figure S4. (a) Raman spectra for the various concentrations of U(VI) stock solutions at pH 5.0. (b) Peak area vs concentration graph as per the data presented in (a).

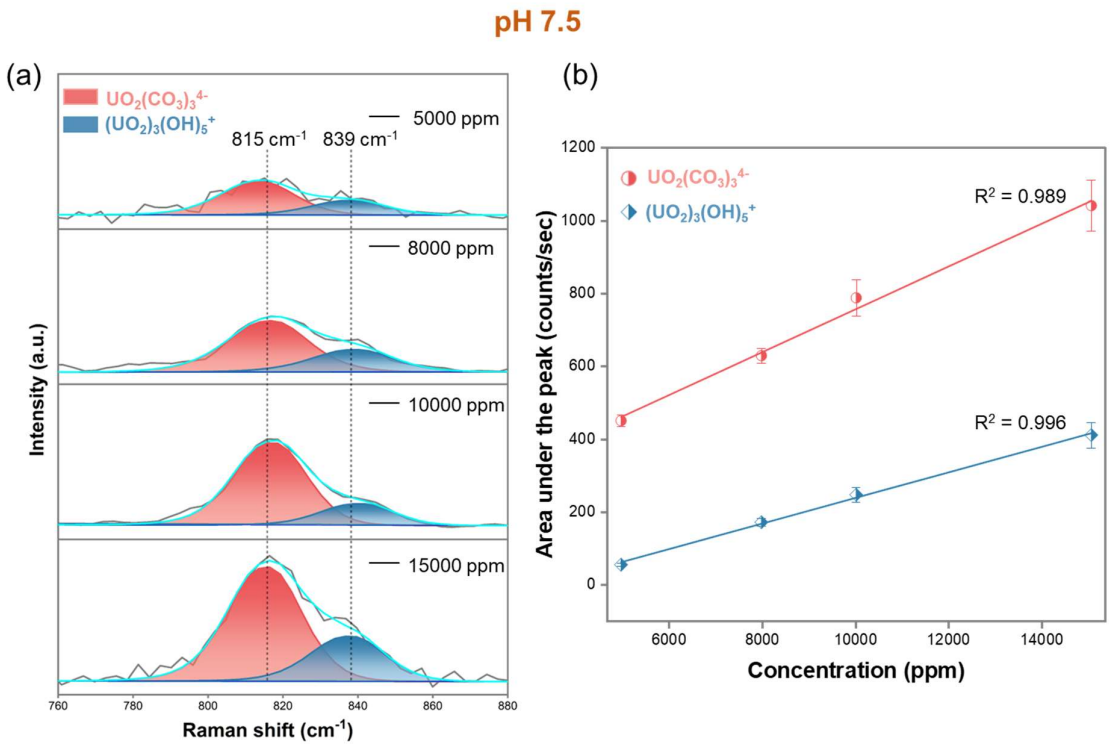

Figure S5. (a) Raman spectra for the various concentrations of U(VI) stock solutions at pH 7.5. (b) Peak area vs concentration graph as per the data presented in (a).

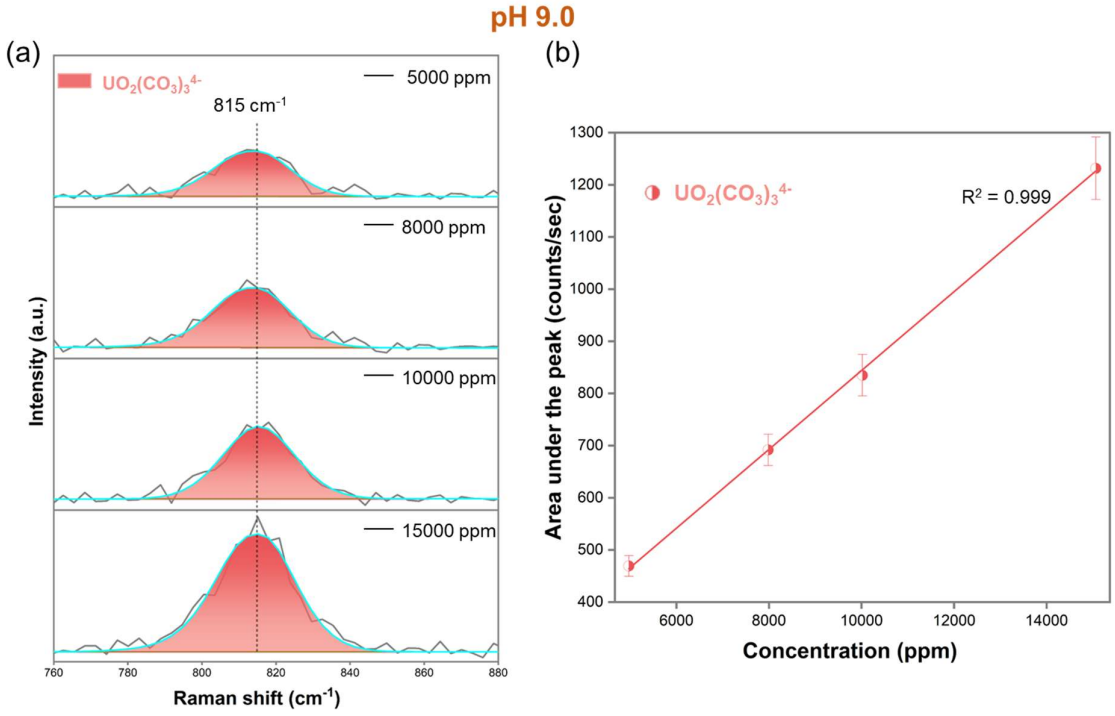

Figure S6. (a) Raman spectra for the various concentrations of U(VI) stock solutions at pH 9.0. (b) Peak area vs concentration graph as per the data presented in (a).

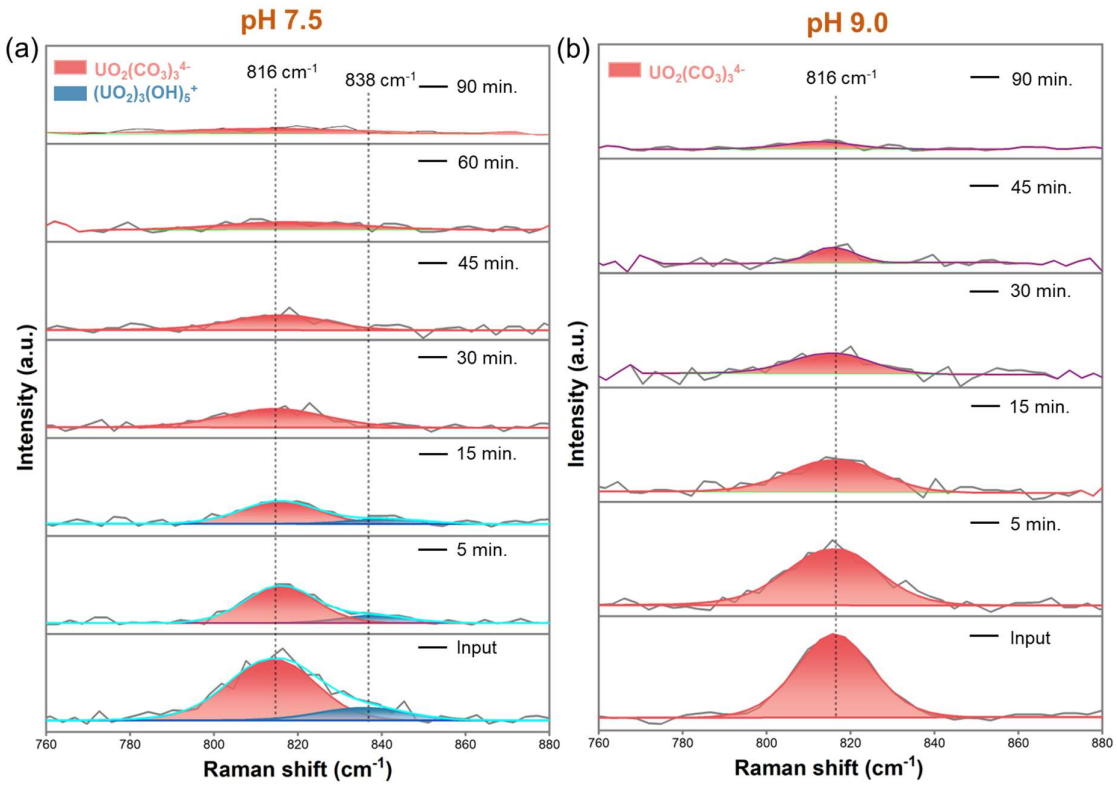

Figure S7. (a) Time-dependent Raman spectra of the interaction of PCNCFH with U(VI) at (a) pH - 7.5 (b) pH - 9.0. Weight of the material taken: 2.5 g. All the Raman spectra were deconvoluted using Casa XPS software.[26]

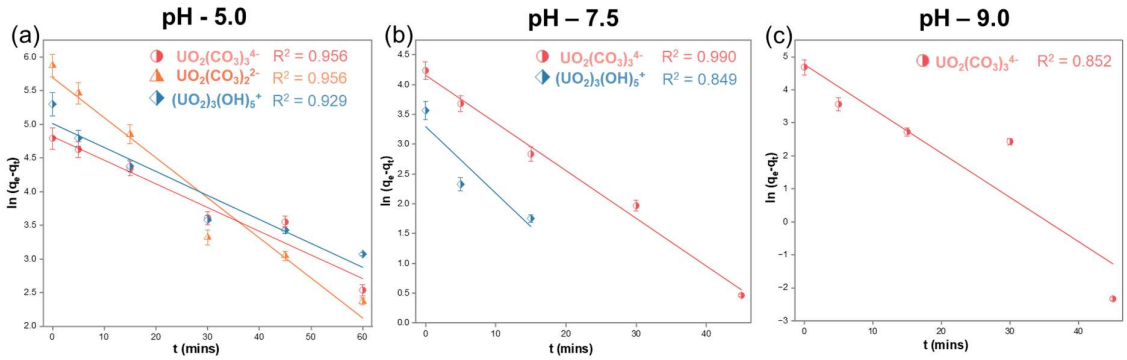

Figure S8. Pseudo-first-order kinetics graph for PCNCFH at (a) pH 5.0, (b) pH 7.5, and (c) pH 9.0.

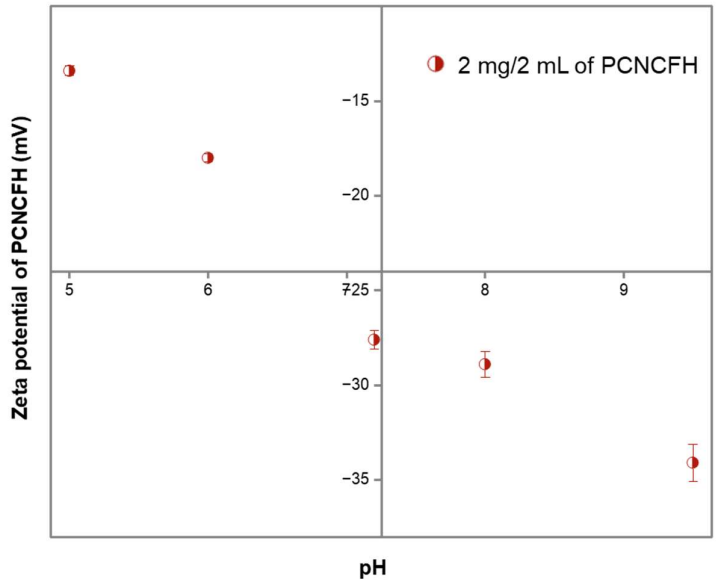

Figure S9. Zeta potential as a function of pH (range 5 -10) for PCNCFH particles in water (2 mg in 2 mL).

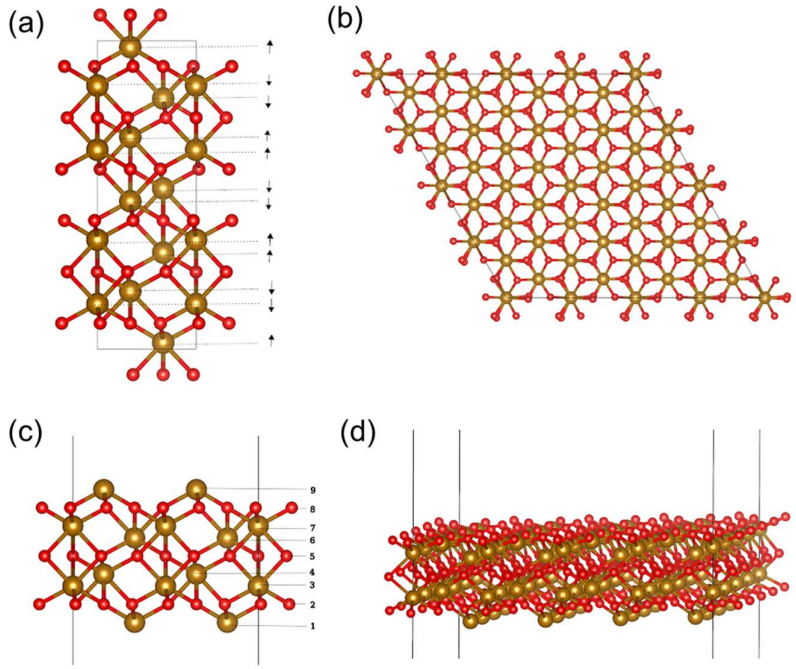

Figure S10. (a) Bulk hexagonal conventional unit cell (containing 6 formula units) of α-Fe_2O_3. The antiferromagnetic spin arrangement, with up and down arrows indicating opposite spin orientations at the Fe sites, that we considered while optimising this system, is shown. (c) Side view of the α-Fe_2O_3(0001) -(2 × 2) slab model (unrelaxed) consisting of nine atomic layers. (b, d) Top and side views, respectively, of the optimized 4 × 4 α-Fe_2O_3(0001) supercell used for the binding energy calculations.

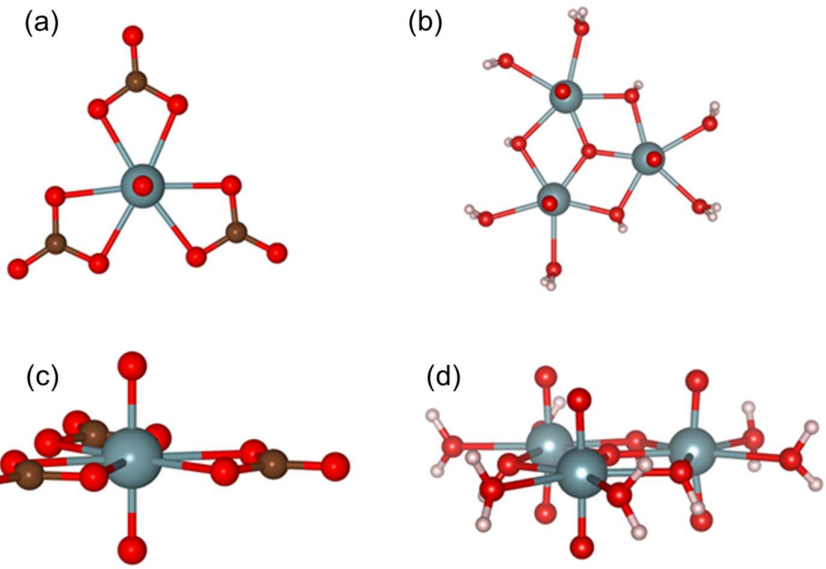

Figure S11. (a, c) Top and side views of the optimised $[UO_2(CO_3)_3]^{4-}$ complex and (b, d) Top and side views of the optimised $[(UO_2)_3(O)(OH)_3(H_2O)_6]^+$ complex.

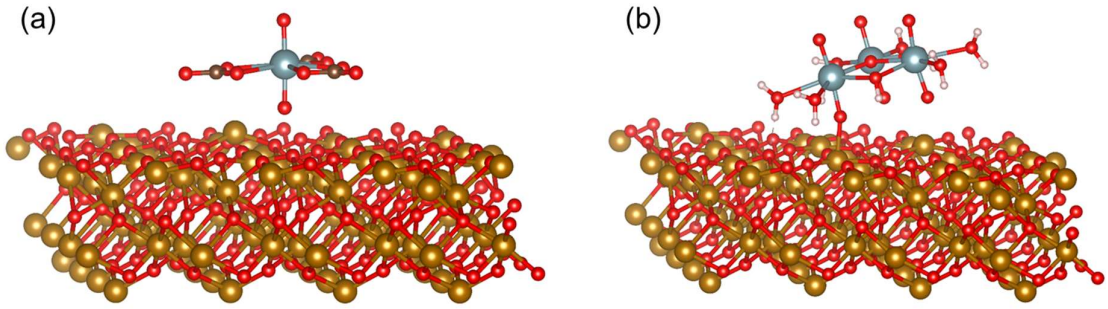

Figure S12. Side views of the optimised (a) $[UO_2(CO_3)_3]^{4-}$ and (b) $[(UO_2)_3(O)(OH)_3(H_2O)_6]^+$ complexes adsorbed onto the α-Fe_2O_3(0001) surface.

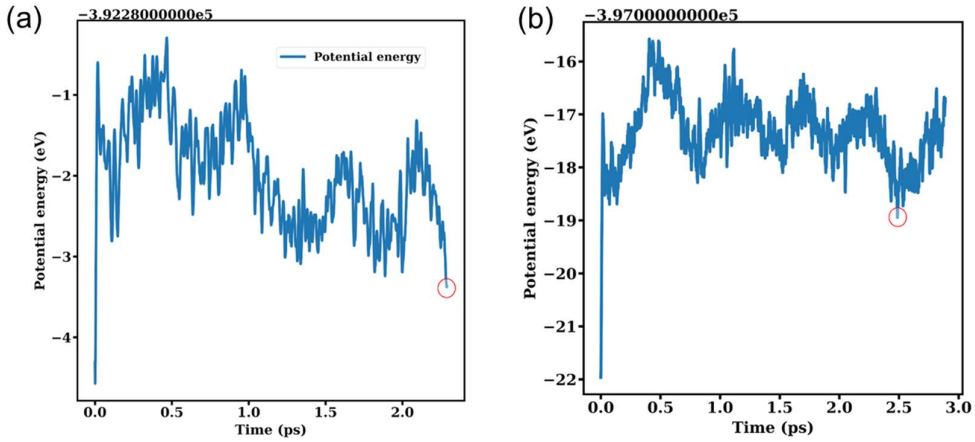

Figure S13. Energy profiles of (a) $[UO_2(CO_3)_3]^{4-}$ and (b) $[(UO_2)_3(O)(OH)_3(H_2O)_6]^+$ complexes adsorbed onto the α-Fe_2O_3(0001) surface. The most stable configurations considered for further optimization are highlighted with a red circle.

Table S1. Comparative U(VI) removal efficiency of PCNC and PCNCFH, calculated from ICPMS data

Adsorbent	Material amount (mg)	Input conc. of U(VI) (ppb)	Output conc. of U(VI) (ppb)	Removal capacity (%)
PCNC	100	9944.05	6745.34	32.16
PCNCFH	100	9100	254.8	97.20

Table S2. Variation of binding energies with Hubbard U for the uranium complexes adsorbed on the α-Fe_2O_3(0001) surface.

Hubbard *U* value	E_{bind} (eV) $[(UO_2)_3(O)(OH)_3(H_2O)_6]^+$	E_{bind} (eV) $[UO_2(CO_3)_3]^{4-}$
Fe (*U* =5), Uranium (*U* =2)	−8.958	−8.659
Fe (*U* =4), Uranium (*U* =2)	−9.173	–8.991
Fe (*U* =4), Uranium (*U* =0)	−9.927	−9.263

Equations used

The correlation between area under the peak and concentration of solution:

$$y = mx + c \qquad \text{Equation (1)}$$

Where, y is area under the peak, x is concentration of the solution (mM), and c is the intercept and m is slope of line of the plot of y versus x. For calculating the unknown concentrations of solution at all pH, the (x,y) data points of line in Figure S3b, Figure S4b and Figure S5b were taken as reference for pH 5.01, 7.53 and 9.01, respectively.

Adsorption kinetics can be expressed by using pseudo-second-order equation:

$$\frac{t}{q_t} = \frac{1}{k_2 q_e^2} + \frac{1}{q_e} t \qquad \text{Equation (2)}$$

q_t (mg/g) and q_e (mg/g) are the amount of adsorbed uranium at particular time t and equilibrium, respectively.

k_2 (g mg^{-1} min^{-1}) is the adsorption rate constant.

Adsorption kinetics can be expressed by using pseudo-first-order equation:

$$\ln(q_e - q_t) = \ln q_e - k_1 t \qquad \text{Equation (3)}$$

q_t (mg/g) and q_e (mg/g) are the amount of adsorbed uranium at particular time t and equilibrium, respectively.

k_1 pseudo-first-order rate constant (min^{-1}).

The maximum uptake of uranium (q_t) by nanocomposites at particular time (t) was determined using the following equation:

$$q_t = (C_o - C_e) * V/m \qquad \text{Equation (4)}$$

where q_t (mg/g) represents the amount of U(VI) species adsorbed per gram of adsorbent at particular time t, C_e is the equilibrium concentration of U(VI) in the bulk solution (mg/L), C_o is the initial concentration of U(VI) (mg/L), V is the volume of the solution (L), and m is the mass of the adsorbent (g).

References

(1) Lu, G.; Haes, A. J.; Forbes, T. Z. Detection and Identification of Solids, Surfaces, and Solutions of Uranium Using Vibrational Spectroscopy. *Coordination Chemistry Reviews* **2018**, *374*, 314–344. https://doi.org/10.1016/j.ccr.2018.07.010.

(2) Lu, G.; Forbes, T. Z.; Haes, A. J. Evaluating Best Practices in Raman Spectral Analysis for Uranium Speciation and Relative Abundance in Aqueous Solutions. *Anal. Chem.* **2016**, *88* (1), 773–780. https://doi.org/10.1021/acs.analchem.5b03038.

(3) Kohn, W.; Sham, L. J. Self-Consistent Equations Including Exchange and Correlation Effects. *Phys. Rev.* **1965**, *140* (4A), A1133–A1138. https://doi.org/10.1103/PhysRev.140.A1133.

(4) Ernzerhof, M.; Scuseria, G. E. Assessment of the Perdew–Burke–Ernzerhof Exchange-Correlation Functional. *The Journal of Chemical Physics* **1999**, *110* (11), 5029–5036. https://doi.org/10.1063/1.478401.

(5) Kühne, T. D.; Iannuzzi, M.; Del Ben, M.; Rybkin, V. V.; Seewald, P.; Stein, F.; Laino, T.; Khaliullin, R. Z.; Schütt, O.; Schiffmann, F.; Golze, D.; Wilhelm, J.; Chulkov, S.; Bani-Hashemian, M. H.; Weber, V.; Borštnik, U.; Taillefumier, M.; Jakobovits, A. S.; Lazzaro, A.; Pabst, H.; Müller, T.; Schade, R.; Guidon, M.; Andermatt, S.; Holmberg, N.;

Schenter, G. K.; Hehn, A.; Bussy, A.; Belleflamme, F.; Tabacchi, G.; Glöß, A.; Lass, M.; Bethune, I.; Mundy, C. J.; Plessl, C.; Watkins, M.; VandeVondele, J.; Krack, M.; Hutter, J. CP2K: An Electronic Structure and Molecular Dynamics Software Package - Quickstep: Efficient and Accurate Electronic Structure Calculations. *The Journal of Chemical Physics* **2020**, *152* (19), 194103. https://doi.org/10.1063/5.0007045.

(6) Blöchl, P. E. Projector Augmented-Wave Method. *Phys. Rev. B* **1994**, *50* (24), 17953–17979. https://doi.org/10.1103/PhysRevB.50.17953.

(7) Hohenberg, P.; Kohn, W. Inhomogeneous Electron Gas. *Phys. Rev.* **1964**, *136* (3B), B864–B871. https://doi.org/10.1103/PhysRev.136.B864.

(8) Goedecker, S.; Teter, M.; Hutter, J. Separable Dual-Space Gaussian Pseudopotentials. *Phys. Rev. B* **1996**, *54* (3), 1703–1710. https://doi.org/10.1103/PhysRevB.54.1703.

(9) Grimme, S.; Antony, J.; Ehrlich, S.; Krieg, H. A Consistent and Accurate *Ab Initio* Parametrization of Density Functional Dispersion Correction (DFT-D) for the 94 Elements H-Pu. *The Journal of Chemical Physics* **2010**, *132* (15), 154104. https://doi.org/10.1063/1.3382344.

(10) Dudarev, S. L.; Botton, G. A.; Savrasov, S. Y.; Humphreys, C. J.; Sutton, A. P. Electron-Energy-Loss Spectra and the Structural Stability of Nickel Oxide: An LSDA+U Study. *Phys. Rev. B* **1998**, *57* (3), 1505–1509. https://doi.org/10.1103/PhysRevB.57.1505.

(11) Tolba, S. A.; Gameel, K. M.; Ali, B. A.; Almossalami, H. A.; Allam, N. K. The DFT+U: Approaches, Accuracy, and Applications. In *Density Functional Calculations - Recent Progresses of Theory and Application*; Yang, G., Ed.; InTech, 2018. https://doi.org/10.5772/intechopen.72020.

(12) Bandyopadhyay, A.; Velev, J.; Butler, W. H.; Sarker, S. K.; Bengone, O. Effect of Electron Correlations on the Electronic and Magnetic Structure of Ti-Doped α -Hematite. *Phys. Rev. B* **2004**, *69* (17), 174429. https://doi.org/10.1103/PhysRevB.69.174429.

(13) Dzade, N.; Roldan, A.; De Leeuw, N. A Density Functional Theory Study of the Adsorption of Benzene on Hematite (α-Fe2O3) Surfaces. *Minerals* **2014**, *4* (1), 89–115. https://doi.org/10.3390/min4010089.

(14) Huda, M. N.; Walsh, A.; Yan, Y.; Wei, S.-H.; Al-Jassim, M. M. Electronic, Structural, and Magnetic Effects of 3d Transition Metals in Hematite. *Journal of Applied Physics* **2010**, *107* (12), 123712. https://doi.org/10.1063/1.3432736.

(15) Grabias, E.; Majdan, M. A DFT Study of Uranyl Hydroxyl Complexes: Structure and Stability of Trimers and Tetramers. *J Radioanal Nucl Chem* **2017**, *313* (2), 455–465. https://doi.org/10.1007/s10967-017-5305-z.

(16) Kotani, A.; Yamazaki, T. Systematic Analysis of Core Photoemission Spectra for Actinide Di-Oxides and Rare-Earth Sesqui-Oxides. *Prog. Theor. Phys. Suppl.* **1992**, *108*, 117–131. https://doi.org/10.1143/PTPS.108.117.

(17) Baer, Y.; Schoenes, J. Electronic Structure and Coulomb Correlation Energy in UO2 Single Crystal. *Solid State Communications* **1980**, *33* (8), 885–888. https://doi.org/10.1016/0038-1098(80)91210-7.

(18) Beridze, G.; Kowalski, P. M. Benchmarking the DFT+ *U* Method for Thermochemical Calculations of Uranium Molecular Compounds and Solids. *J. Phys. Chem. A* **2014**, *118* (50), 11797–11810. https://doi.org/10.1021/jp5101126.

(19) Johansson, B. Nature of the 5 f Electrons in the Actinide Series. *Phys. Rev. B* **1975**, *11* (8), 2740–2743. https://doi.org/10.1103/PhysRevB.11.2740.

(20) Herbst, J. F.; Watson, R. E.; Lindgren, I. Coulomb Term U and 5 f Electron Excitation Energies for the Metals Actinium to Berkelium. *Phys. Rev. B* **1976**, *14* (8), 3265–3272. https://doi.org/10.1103/PhysRevB.14.3265.

(21) Martínez, L.; Andrade, R.; Birgin, E. G.; Martínez, J. M. P ACKMOL : A Package for Building Initial Configurations for Molecular Dynamics Simulations. *J Comput Chem* **2009**, *30* (13), 2157–2164. https://doi.org/10.1002/jcc.21224.
(22) Nosé, S. A Molecular Dynamics Method for Simulations in the Canonical Ensemble. *Molecular Physics* **2002**, *100* (1), 191–198. https://doi.org/10.1080/00268970110089108.
(23) Hoover, W. G. Canonical Dynamics: Equilibrium Phase-Space Distributions. *Phys. Rev. A* **1985**, *31* (3), 1695–1697. https://doi.org/10.1103/PhysRevA.31.1695.
(24) Humphrey, W.; Dalke, A.; Schulten, K. VMD: Visual Molecular Dynamics. *Journal of Molecular Graphics* **1996**, *14* (1), 33–38. https://doi.org/10.1016/0263-7855(96)00018-5.
(25) Humphrey, W.; Dalke, A.; Schulten, K. VMD: Visual Molecular Dynamics. *Journal of Molecular Graphics* **1996**, *14* (1), 33–38. https://doi.org/10.1016/0263-7855(96)00018-5.
(26) Fairley, N.; Fernandez, V.; Richard-Plouet, M.; Guillot-Deudon, C.; Walton, J.; Smith, E.; Flahaut, D.; Greiner, M.; Biesinger, M.; Tougaard, S.; Morgan, D.; Baltrusaitis, J. Systematic and Collaborative Approach to Problem Solving Using X-Ray Photoelectron Spectroscopy. *Applied Surface Science Advances* **2021**, *5*, 100112. https://doi.org/10.1016/j.apsadv.2021.100112.